1

ON THE DETERMINATION OF DIFFUSION COEFFICIENTS IN TWO-COMPONENT ALLOYS AND DOPED SEMICONDUCTORS. SEVERAL IMPLICATIONS CONCERNING THE INTERNATIONAL SPACE STATION

O. Sanchez[1] , X. Ruiz[2,3], M. Pujalte[2], I. Mercader[1], O. Batiste[1], Jna. Gavaldà[2]

([1]) Departament de Física Aplicada, Universitat Politècnica de Catalunya, UPC. Barcelona. Spain.
([2]) Departament de Química Física i Inorgànica, Universitat Rovira i Virgili, URV, Tarragona,
([3]) Institut d'Estudis Espacials de Catalunya, IEEC, Barcelona, Spain.

ABSTRACT

The accurate determination of interdiffusion coefficients is a technologically relevant problem that has implications on the correctness of the predictions when using the existing models of solidification. It is also important in the validation of different theories of atomic diffusion. The experimental determination of these coefficients when there is a liquid phase is difficult due to the unavoidable presence of buoyancy driven convection currents that enhance mass transport and disturb diffusion measurements. To minimize as much as possible these problems, long capillaries are used in order to confine the fluid and reduce the intensity of the convective motions. More recently, these measurements have been done in reduced gravity environments, but the residual gravity is still able to induce buoyancy driven convection motions. The aim of our work is to numerically analyze the impact of low and moderate Rayleigh number environments on the accuracy of the interdiffusion coefficient measurements using long capillaries. In the present study we deal with two liquid systems; photovoltaic silicon and Al-based liquid binary alloys at high temperature. We have numerically simulated in 3D two different experimental techniques used to determine the diffusion coefficients, this extends previous reported 2D calculations. We also consider the effect of rotating the cylindrical cell along their axis as a general stabilization mechanism of the convective motions. Finally, we use typical accelerometric signals from the International Space Station (ISS) in the quasi-steady range of frequencies. The signals concentrate on typical station reboosts because of the accelerometric level of the rest of disturbances –dockings, undockings and Extra Vehicular Activities, EVAs- is considerably lower.

NOMENCLATURE

A   amplitude

C   concentration of the denser component

C_i averaged concentration in segment i

ΔC^* difference between maximum and minimum concentration at t = 0 [mol m^{-3}]

D   diffusion coefficient [m^2 s^{-1}]

$D^*(t)$ apparent diffusion coefficient [m^2 s^{-1}]

$\%D^*(t)$ standard nondimensional indicator

$\%D^*(t_{end})$ uncorrected final indicator at the end time

$\%D^*_{diff}(t_{end})$ zero error due to the methodology used (diffusive case at the end time)

$\%D(t_{end})$ corrected nondimensional indicator at the end time

$< E_k >$ mean kinetic energy

g   microgravity level [m s^{-2}]

H   height of the rectangular domain [m]

L   capillary cell length [m]

p   pressure

R   radius of the cylinder [m]

$\vec{Ra}$ solutal Rayleigh number ($\vec{Ra} = \dfrac{\vec{g}\,\beta_c\,\Delta C^*\lambda^3}{\nu\,D}$)

Sc   Schmidt number (Sc = υ/D)

t   time

t_{end} end time

$\vec{V}$ velocity field

x, y, z   Cartesian coordinates

r, θ, z   cylindrical components

z_i axial position of the center of the shear cell segment i

3

Greek letters

α   angle between the gravity vector and the gradient of concentration

β_c solutal expansion coefficient [m^3 mol^{-1}]

Γ   aspect ratio

λ   length scale

υ   kinematic viscosity [m^2 s^{-1}]

f   nondimensional external frequency

Ω   nondimensional axial angular velocity

τ   time scale

τ_i thruster ignition time

1. INTRODUCTION

The accurate determination of the diffusion coefficients in high temperature doped melts and also in two-component liquid mixtures is very important for its further implications in the knowledge and control of generic solidification processes. In effect, diffusion coefficients are usually treated as constants in computational growth models, but real systems with large segregation coefficients need the consideration of concentration and position dependent diffusion coefficients because of the strong gradients existing at the growing interfaces. In addition, concentration gradients are correlated with chemical potential gradients, so it is very important to deep also in the determination and understanding of such relationships in order to be properly applied in predictive growth models. The experimental determination of the diffusion coefficients is also important from a theoretical perspective in order to validate different diffusion theories predicting how theses coefficients depend on temperature and concentration.

Diffusion coefficients at high temperature are usually measured on Earth laboratories typically using diffusion couple arrangements inside long capillaries. The initial concentration profile, a step, is left to diffuse later during a certain time. The final concentration profile is compared to the analytical solution obtained using Fick's law and the required diffusion coefficient compatible with this profile is calculated [1, 2]. In order to preserve diffusion from potential disturbances consequence of the melting and solidification processes, the capillary is divided in slices that can be individually moved perpendicular to their axis (shear cell technique, SC hereafter). In this way, when the diffusion process is stopped and the slices are separately cooled until they solidify, the concentration of each solidified slice enable to accurately reconstruct the final concentration profile needed (*post mortem* analysis) [3]. Recently, a direct procedure using X-ray radioscopic techniques (capillary technique, XR hereafter) allows *in-situ* instantaneous measurements of the concentration profiles by taking absorption pictures of the experiments [4 - 6]. Despite this technique is not universal, a number of high temperature liquid systems could fortunately be processed in this way. Also, there exist other less popular possibilities as the so-called Axial Heat Processing, AHP. Strictly speaking, this is a crystal growth methodology which tries to control thermal conditions near the growing interface to minimize natural convection. The segregation in the solid grown phase is then used as a basis for the subsequent diffusion analyses [7 - 11].

During the last years space environments has also been used to estimate ultra-accurate interdiffusion coefficient measurements. But again a difficult factor to control there is the effect of low accelerations which are potential sources of residual convective contamination [12 - 15]. To assess the real importance of such effects, the acceleration environment must be characterized in detail and numerical models will then be used to carefully evaluate the flow impact on diffusion measurements. This is exactly the aim of the present work. Our methodology will consist in performing numerical simulations of the capillary cells and compare the final states with the expected ones by a pure diffusive process without convection. As it has been mentioned before, in shear cell simulations the comparisons will use the averaged concentration of each one of the segments of the cell while that in the simulation of the X-ray radioscopic techniques we will use the continuous concentration profiles all along the capillary. The present numerical experiments can manipulate both types of concentration measurements without problems.

Due to their unquestionable technological interest we focus the study on two different kinds of materials, photovoltaic silicon (PV-Si) and aluminum based alloys. Concerning multi-crystalline ingots of photovoltaic silicon, PV-Si, the knowledge of the diffusion coefficients of dopants and impurities is of capital importance to improve the predictions of the present computational models of directional solidification [16 - 25]. Remember that, for economic reasons, that is to say, to attain parity (cost of solar energy equal to costs of conventional energy sources), Upgraded Metallurgical Grade Silicon, UMG-Si, is progressively replacing the more expensive ultra pure Electronic Grade Silicon, EG-Si, as feedstock material in ingot casting processes. But, UMG-Si contains a high amount of the above-mentioned dopants, metallic and non-metallic impurities which strongly interact with crystal defects in the resulting multi-crystalline ingots (see Table 1). Concerning metallic

alloys, in particular, Al-based alloys, diffusion and their relation to thermodynamics play a capital role in nucleation theories and in the correct predictions of the coupled macro-meso-microscopic computational models of solidification [26 - 28].

Metallic impurities (Al, Bi, Ga, In, ...)		UMG-Si feedstock	Point defects (scarcely incorporated during solidification because of the very low values of their segregation coefficients)	Decreasing of efficiency due to minority carriers (electrons) recombination
Non-metallic impurities	O	UMG-Si feedstock (SiO$_2$ particles) (dissolution of SiO$_2$-crucible in mono-crystalline Czochralski growth)	Oxide and silicide particles could act as getter centers for metallic impurities	Degradation of the solar cell during illumination Decrease of the electric properties
	C	Graphite heaters (CO in the near atmosphere)	Formation of SiC clusters (evaporation of SiO$_2$ at the melt surface)	SiC clusters can act as electrical shunts (also, wire breakings during the wire sawing process)
	N	Si$_3$N$_4$ coating of fused silica crucibles (dissolution of the Si$_3$N$_4$ layer)	Si$_3$N$_4$ formation (acting as nuclei for SiC clusters)	

Table 1. Effect of dopants, metallic and non-metallic impurities in the obtaining of PV-Si

The paper is organized as follows: in Section 2 we will describe the governing equations and the numerical methods used, in Section 3 the results corresponding to typical low and moderate solutal Rayleigh number environments (Section 3.a) as well as the ones corresponding to real accelerometric records coming from the International Space Station (Section 3.b) will be presented. Finally the conclusions of the study will be summarized in Section 4.

2. GOVERNING EQUATIONS AND NUMERICAL PROCEDURES

To model the problem we use either a rectangular 2D domain or a 3D closed cylinder, filled with a two-component liquid mixture. Due to the fact that the furnaces used in real experiments at high temperature have a very low thermal gradient, we consider the thermal effects negligible focusing on the resolution of the solutal problem. We consider the configuration so-called interdiffusion couple [2]. In this case the diffusion is driven by the existence of two half parts with different initially uniform concentrations, located symmetrically at both sides of the cell. This system is analyzed using the transport equation for mass coupled to the incompressible Navier–Stokes equations in the Boussinesq approximation. In this way we are able to consider the effect of the convection currents induced by the density variations caused by concentration differences. The equations written in nondimensional form are

$$\nabla \cdot \vec{V} = 0 \tag{1.a}$$

$$\frac{\partial \vec{V}}{\partial t} + (\vec{V} \cdot \nabla)\vec{V} = -\nabla p + \text{Sc}\,\nabla^2 \vec{V} - \overrightarrow{\text{Ra}} \cdot \text{Sc} \cdot C \tag{1.b}$$

$$\frac{\partial C}{\partial t} + \vec{V} \cdot \nabla C = \nabla^2 C. \tag{1.c}$$

Here $\vec{V}$ is the non-dimensional velocity and C is the concentration of the denser component. The length scale λ used to obtain the previous non-dimensional variables is the height ($\lambda = H$) in the rectangular domain and the diameter ($\lambda = 2R$) in the cylindrical one. The time scale τ is the dimensional group λ^2/D, being D the mass diffusion coefficient. The non-dimensional concentration is defined as, $C = (C^*-C_o^*)/\Delta C^*$ where ΔC^* is the initial concentration difference and C_o^* is it's mean value. Other parameters appearing in the equations are the vector solutal Rayleigh number $\overrightarrow{Ra}$, and the Schmidt number Sc, respectively defined as

$$\overrightarrow{Ra} = \frac{\vec{g}\,\beta_c\,\Delta C^*\lambda^3}{\nu\,D}, \qquad Sc = \frac{\nu}{D},$$

where β_c is the solutal expansion coefficient, ν is the kinematic viscosity and $\vec{g}$ is the gravity vector. In the cylindrical cell the coordinate system of the problem has been chosen in such a way that the positive z axis coincides with the axis of the cylinder and the origin of coordinates is on the center of the basis of the cylinder (see Fig. 1). Mention that in non-dimensional variables the length L of the rectangular or the cylindrical cell is defined by its aspect ratio, $\Gamma = L / H$ or $\Gamma = L / 2R$, respectively. In the present calculation the aspect ratio is chosen $\Gamma= 40$ in both rectangular and cylindrical non-dimensional domains.
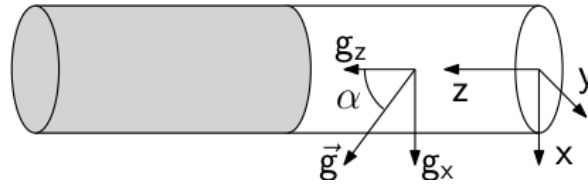
Fig. 1. Sketch of the long cylindrical capillary with the initial diffusion couple.

Table 2 defines the typical quantitative values for the two materials considered, photovoltaic silicon and aluminum-based alloys, taking into account real values extracted from the specialized literature, that is to say references [29 – 32] for PV-Si and references [33 – 36] for aluminum-based alloys. All these values have been considered constant, i.e. independent on the composition. To accomplish this last hypothesis, the initial quantitative difference between the concentrations of both sides of the cell has been limited to a reasonable threshold value of the order of 5 wt%. Also Table 2 shows the geometrical values needed to dimensionally define the computational domain, the length, L, the height (H) and the diameter (2R) respectively.

Symbol	Units	Photovoltaic Si	Al-based alloy
L	cm	6	6
H (2R)	cm	0.15	0.15
$10^3\,\upsilon$	cm^2 s^{-1}	3	3
$10^4\,D$	cm^2 s^{-1}	1	0.2
$10^2\,\beta_c\,(c-c_0)$	-	0.5	- 1

Sc	-	30	150
10^3 Ra (values at 1 μg)	-	56.25	562.5

Table 2. Typical thermophysical properties of the two binary fluids considered here.

The numerical solution of the above-mentioned transport equations has been obtained using different methods and schemes. Concerning 2D calculations, two different finite volume schemes have been used. The first one, (2D/S1), uses a second-order central scheme for the spatial discretization of the diffusive and convective terms and it performs the time integration using a Crank–Nicolson scheme. The coupling between the velocity and pressure fields is solved with a fractional step method and the resulting Poisson equation is solved using the biconjugate gradient method [1-2, 37]. The second scheme, (2D/S2), is similar but to solve the coupling between the pressure and velocity fields uses the SIMPLE method. The resulting equation for the pressure correction is then solved using a multigrid algorithm [38]. Concerning 3D calculations, a finite volume and a pseudospectral method have also been used in order to model the two different experimental techniques, SC and XR respectively. The main features of the 3D finite volume code, are identical to the (2D/S2) ones. The pseudospectral method uses the algorithm described in [39] that can be summarized as follows. To integrate the equations in time, we use the second order time-splitting method proposed in [40] which employs a pressure boundary condition, which in conjunction with stiffly stable schemes prevents propagation and accumulation of time difference errors [41]. For the spectral spatial discretization, we use a Galerkin-Fourier method in the azimuthal direction and Chebyshev collocation in radial and axial directions. The radial dependence of the functions is approximated by a Chebyshev expansion between -R and R, but forcing the proper azimuthal parity of the variables at the origin [42, 43]. For instance, the concentration field and the axial component of the velocity have an even parity, whereas the radial and azimuthal components of the velocity field are odd functions. To avoid including the origin in the mesh grid, we use an odd number of Gauss-Lobatto points in the radial direction, and we enforce the equations only in the interval (0,R]. For each Fourier mode, these equations are solved using a diagonalization technique in the two coordinates r and z. The imposed parity of the functions guarantees the regularity conditions at the origin needed to solve the Helmholtz equations [40].

Concerning finite volume meshes say that in all 2D runs we have used 91000 rectangular control volumes slightly graded toward the walls and the initial line of separation between the two regions with different concentrations [1, 2]. In all 3D runs, a total number of about 610000 control volumes were needed to obtain correctly converged results. Typical time steps in these cases are of the order of 10^{-5}. Pseudospectral mesh with $nr = 42$, $nz = 301$ and $n\theta = 20$ points for radial, axial and azimuthal directions, with a time step of 10^{-3}, suffices to obtain converged results in all computations. Mention here that, in addition to the corresponding convergence checking effected in each particular case [1, 2], [37], [39], the coincidence of the results obtained with the different schemes can also been interpreted as an additional indirect probe of the correctness of the present reported results.

With respect to boundary conditions, the walls of both the shear cell and the long capillaries have been defined as no-slip and impermeable boundaries. Initial starting values consider uniform fields in the entire domain at rest. At this respect notice that the interdiffusion configuration used here define constant initial values of concentration of -0.5 and +0.5 respectively at both sides of the couple. This initial condition is easily accomplished in the finite volume case but in the pseudo spectral code the abrupt central discontinuity has been approximated by a hyperbolic tangent profile $C(0, r, \theta, z) = 0.5\tanh\left[\delta\left(2\,\Gamma^{-1}z - 1\right)\right]$, where $z = [0, \Gamma]$ with Γ the aspect ratio of cylinder. The parameter δ was chosen as 300 for $nz = 301$.

The numerical results of the transport equations have then been post-processed trying to mimic each one of the two different experimental procedures reported in the literature for the obtaining of the different diffusion coefficients. In the first case – the "post-mortem" chemical analyses- the shear cells are considered to be formed by slices which, conveniently solidified, are analyzed at the end of the experiment to give an average final value of concentration. In the second case – the "in situ" X-ray analysis- the source of information comes from the instantaneous profiles of gray level all along the capillary. In both experimental procedures an estimated value of the diffusion coefficient $D^*(t)$ is obtained from the comparison of the numerical results with the analytical transient solution of the one dimensional diffusive problem with a constant diffusion coefficient in an infinite domain $C(t, r, \theta, z) = -\frac{1}{2} \cdot \mathrm{erf}(-\frac{z}{2 \cdot \sqrt{D \cdot t}})$, where erf is the error function.

The "post-mortem" indirect procedure has been modeled in all 2D and 3D calculations effected by using the finite volume method. We define here a standard cell with 20 slices that, in terms of absolute measures, have a diameter of 0.15 cm and a length of 0.30 cm. The mathematical post-processing is similar to the one presented in refs. [1, 2] so, the determination of $D^*(t)$ involves the calculation of the slope of the set of points $\{(z_i, 2 \cdot \sqrt{t} \cdot \mathrm{erf}^{-1}(-2 \cdot C_i(t, z_i), \forall i = 1, 20\}$ by linear fitting. In this expression z_i is the position of the centre of each segment of the cell, t the corresponding time, erf^{-1} the inverse of the Gauss error function, $C_i(t, z_i) = \frac{1}{S_i} \cdot \iint C(t, x, z) \, dS$ the segment-averaged computed concentration in the 2D case and $C_i(t, z_i) = \frac{1}{V_i} \cdot \iiint C(t, r, \theta, z) \, dV$ the similar segment-averaged computed concentration but in the 3D case. Calculations of $D^*(t)$ used only active segments in which the variation of the averaged concentration is greater than the 1% of the initial value. This choice is consistent with the 1% error threshold associated with the determination of the averaged concentration of each solidified slice of the shear cell by usual solid state techniques as, for example, Atomic Absorption Spectroscopy, Secondary Ion Mass Spectroscopy or Electron Probe Micro Analysis.

The "in situ" direct X-Ray methodology has been based on the pseudospectral method. The concentration values $C(t, r, \theta, z)$ obtained in each time step are cross-section averaged $\overline{C}(t, z)$ at each collocation point along the z-axis. After that we fit a concentration profile $(z, \overline{C}(t_{end}, z))$ to the error function profile by minimizing the least-squared error. $D^*(t)$ is finally calculated from the fit parameters. The evaluation of the error –in percentage- finally defines, in both cases, the following standard nondimensional indicator [14, 15],

$$\%D^*(t) = 100 \cdot \frac{D^*(t) - D}{D} = 100 \cdot \left\{ \frac{D^*(t)}{D} - 1 \right\} \tag{2}$$

In order to satisfy the mathematical hypothesis of infinitely long domains, in the first case ("post-mortem" indirect procedure) calculations finished when the first and last segments become simultaneously active. The time needed to attain these final conditions is called the end time, t_{end} and the final error associated to the process is $\%D^*(t_{end})$. In the second case ("in situ" direct procedure) the calculations finished when the averaged concentration in the z-axis first and last points, corresponding to the lids, also change more than 1% with respect to the initial value. These computational strategies avoid, in both cases, the necessity to consider the end time as a parameter to be simultaneously determined during the experiments, as really occurs. Notice that the end times of both procedures will be slightly different.

Additional information concerning the purely diffusive case, equivalently, the vertical stable configuration, shows that the quantitative value of the final indicator $\%D_{diff}^{*}(t_{end})$ in both procedures is low, of the order of 1.5, but not strictly zero. This value has been considered as a zero error inherent to the numerical methodology used and systematically subtracted from the $\%D*(t)$ in each case. So, the corrected final indicator results as,

$$\%D(t_{end}) = \%D*(t_{end}) - \%D_{diff}^{*}(t_{end}) \qquad (3)$$

3. RESULTS AND DISCUSSION

3.1. Typical low and moderate solutal Rayleigh number environments

Fig. 2 displays the relative error in the determination of the diffusion coefficient $\%D(t_{end})$ as a function of the solutal Rayleigh number in the case in which the gravity and the initial density gradient are orthogonal. The results for the two values of the Schmidt numbers considered, 30 and 150, are practically identical and so only the calculations for Sc=150 are plotted. The 2D results obtained with the two methods SC(2D/S1) and SC(2D/S2) are roughly coincident and, independently on the numerical scheme used [14, 15], a quadratic tendency is observed. The difference between the values of $\%D(t_{end})$ at $Ra = 1500$ is of the order of 0.3. With respect to the 3D results, the presence of bounded walls in the third dimension introduces friction, which slows the convective motions produced by the interaction between the gradient of density and the orthogonal gravity. This fact promotes, in comparison with 2D results, higher values of the end time, t_{end}, and also $\%D(t_{end})$ values considerably lower [1,2]. If we compare the 3D results for the two techniques, 3D finite volume simulations in a cylinder modeling a 20 slices shear cell, SC(3D), and 3D pseudospectral method modeling the X-Ray technique, XR(3D), we obtain different end times (see Fig. 3) and a difference in $\%D(t_{end})$ of the order of 0.25 at Ra = 1500. Nevertheless it must be cautious with this last value because in 3D calculations the difference could have two origins, the numerical scheme and the slightly different post-processing methodology. However, as it is shown in the insets of Fig. 2 and of Fig. 3, increasing the number of slices, the numerical results of SC tends to the XR ones. Therefore it is clear that the different numerical techniques are not the origin of the differences observed. The results show that the indirect postmortem method and the direct X-Ray methodologies are very similar but not totally equivalent. In addition, the results also show that, in the orthogonal case, tridimensional considerations are mandatory in a more realistic discussion of the problem. In this way, the experimental threshold limit of the 1%, is around Ra = 625 in the 2D case but in the 3D case the value changes to be roughly twice, Ra = 1250. This means that, in terms of gravity values, the realistic threshold is located now around 1 mg. This change in the g level ensures a wider security range in which the experiment, located orthogonally, will present insensitivity to these kind of constant microgravity levels.
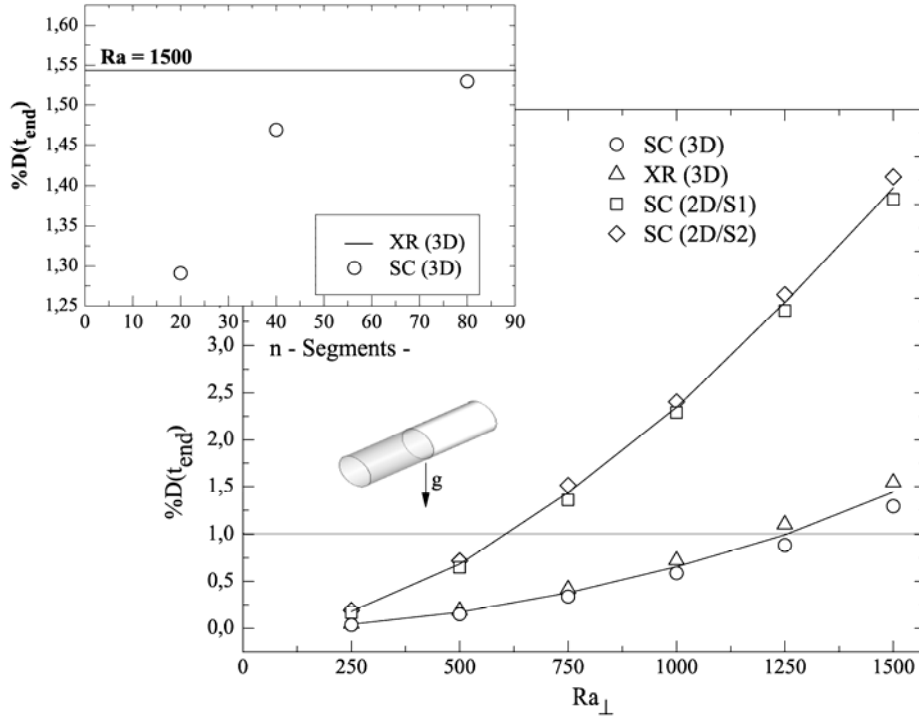
Fig. 2. Variation of the %D(t_{end}) values as a function of the solutal Rayleigh number for different two and three-dimensional computational schemes (gravity is acting orthogonally to the gradient of concentration in all cases). Also shown the %D(t_{end}) for different number of segments of the shear-cell, and for the XR case for Ra=1500.
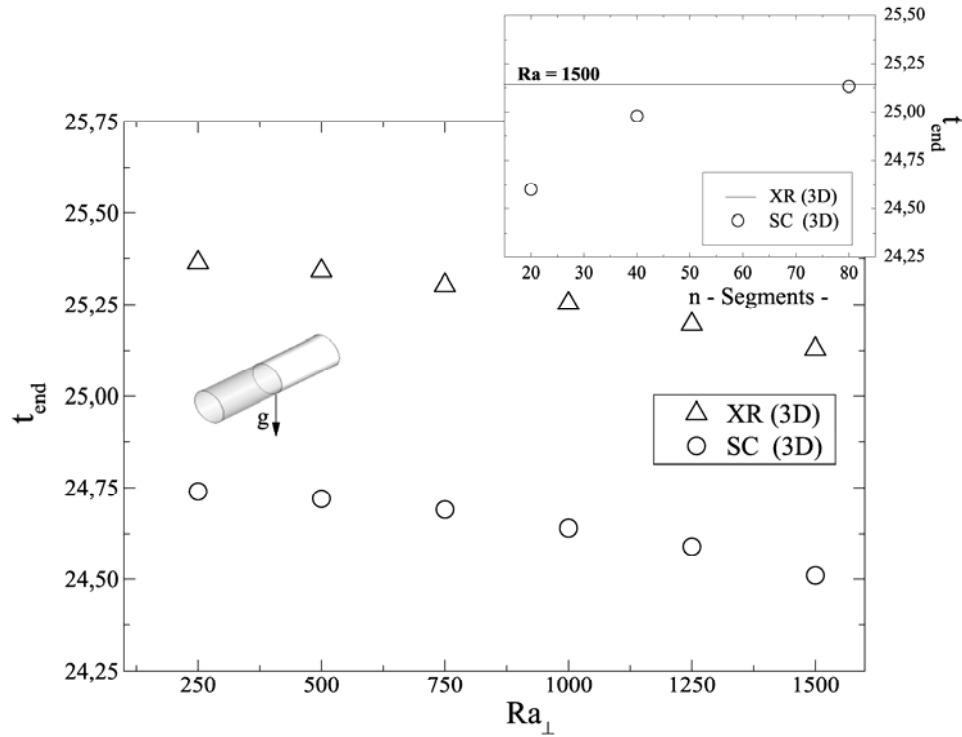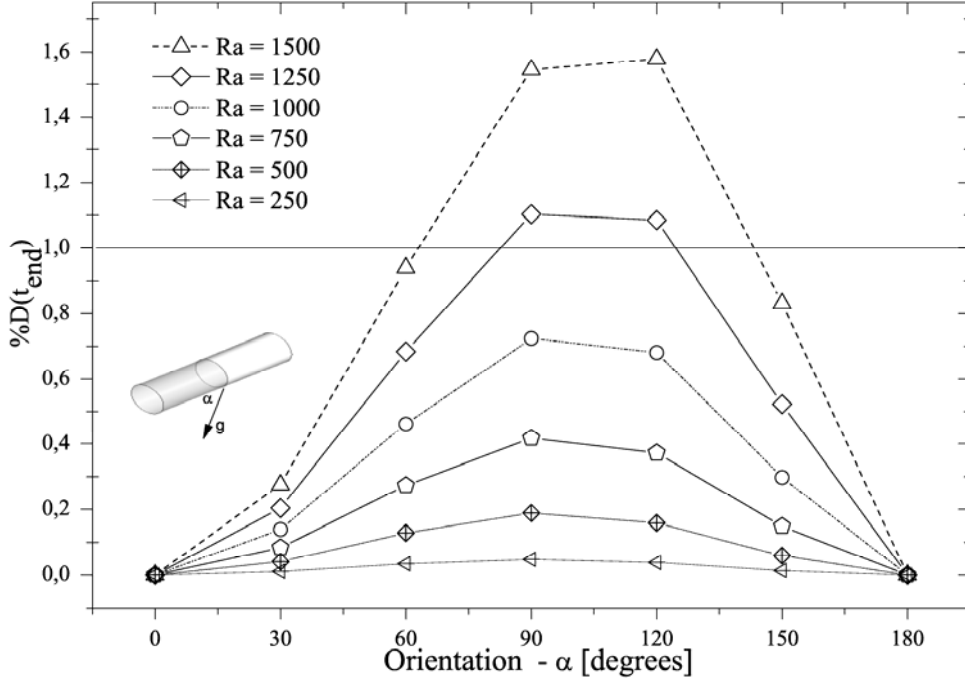

Fig. 3. Variation of the t_{end} values as a function of the solutal Rayleigh number for different three-dimensional computational schemes (gravity is acting orthogonally to the gradient of concentration in all cases). Also shown the t_{end} for different number of segments of the shear-cell, and for the XR case for Ra=1500.

Another important consideration to be effected in spacecrafts concerning the determination of %D(t_{end}) is the orientation of the gravity vector against the direction of the initial density gradient (see Fig. 1). For a gravity vector $\vec{g} = g_x\vec{i} + g_z\vec{k}$ g or equivalently, $\overrightarrow{Ra} = Ra_x\vec{i} + Ra_z\vec{k}$, the initial driving is produced by the interaction between the initial concentration profile C(0,z) and the g_x component of the gravity vector only. Once the initial profile of concentration is perturbed, an interaction of this perturbation with the g_z component arise, being its effect on the driving term dependent on the sign of g_z. If $g_z > 0$ (α < 90º) the initial driving is damped, in favor of the pure diffusive process, but if $g_z < 0$ (α > 90º) the initial driving is enhanced, in favor of the convective contamination. Therefore this nonlinear secondary effect depends on both components of the vector Rayleigh number, equivalently, on both components of the gravity vector. To clearly show this effect we present in Fig. 4 the time evolution of the mean kinetic energy in a cylindrical cell for instants close to t=0. The calculations have been done using the pseudospectral method only modeling the X-Ray methodology. Three pairs of values of the Rayleigh numbers and orientations (Ra, α) with the same value of the x-component, $Ra_x \approx 1299$, have been chosen: $(1500, 60^0)$, $(1500, 120^0)$, $(1299, 90^0)$. In all of them the initial driving is the same, but the immediate interaction with the z-component, Ra_z, is different. In case of enhancing, the secondary nonlinear effect can even overcome a higher initial driving. This is what happens for example with the results for $(1500, 90^0)$ also shown in the same Fig. 4.
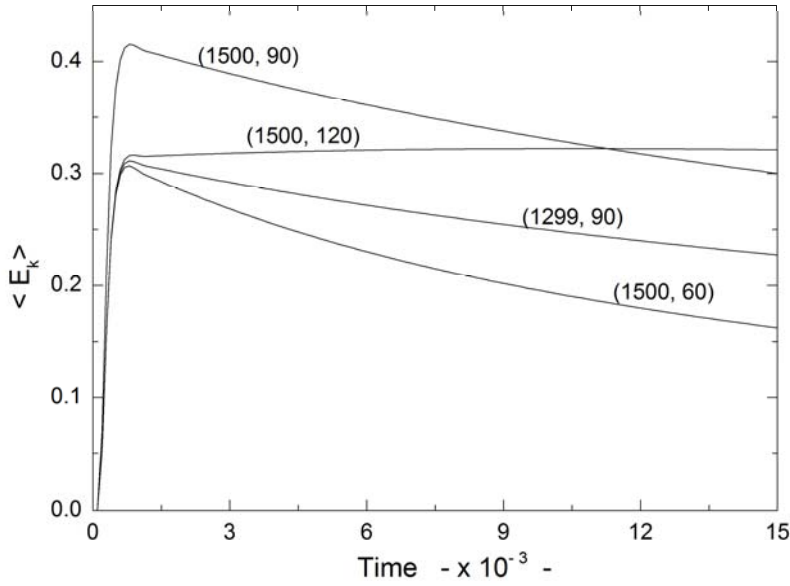
Fig. 4. Time evolution of the mean kinetic energy in a cylindrical cell for instants close to t=0. Three pairs of values of the Rayleigh numbers and orientations (Ra, α) with the same value of the x-component $Ra_x \approx 1299$ have been chosen: $(1500, 60^0)$, $(1500, 120^0)$, $(1299, 90^0)$. Results for $(1500, 90^0)$ have also been included for comparison.

Fig. 5 shows the relative error in the determination of the diffusion coefficient %D(t_{end}) as a function of the orientation α for different values of the solutal Rayleigh number. The results correspond to a cylindrical cell and have been obtained by using a spectral method modeling the X-Ray direct methodology. Again, the results for the two values of the Schmidt number considered, 30 and 150, are coincident. The results indicate that, according to the previous discussion, the relative error is asymmetric respect the orthogonal position.

Clearly if the solutal Rayleigh values increases the asymmetry degree becomes more pronounced. Therefore, the position of the maximum value of the different %D(t_{end}) curves, as the solutal Rayleigh number increases, shifts towards α = 180º. For the values of the solutal Rayleigh number of the figure, at the point α = 180º the values of %D(t_{end}) are practically zero because the Rayleigh number based on the length of the diffusion layer is below the critical value for the onset of convection, i.e., no gravity-induced mixing exists. In the other side of the scale, α = 0º, the values of %D(t_{end}) go to zero according to the definition in equation (3).


Fig. 5. Variation of the %D(t_{end}) values as a function of the relative orientation α between the gradient of concentration and the constant gravity vector, for different values of the Rayleigh number. The 1% experimental limit is also plotted for comparison.

The impact of the vibrations on the different experiments is another extremely relevant problem in all kind of spacecrafts. To analyze it, we consider here only the simplest ideal model in which gravity is a harmonic function of time, that is to say, $g(t) = A\cos 2\pi f t$, acting orthogonally to the initial density gradient generated by the concentration step profile. Fig. 6, shows the values of %D(t_{end}) as a function of the external frequency f applied for two values of the Rayleigh number 1500 and 3000, evaluated using the value of the maximum gravity amplitude A. The results have been obtained using the 3D pseudospectral scheme modeling the X-Ray direct methodology. Independently on the value of the Schmidt number, calculations show that for the different vibrational Rayleigh numbers considered a well-defined inflexion point appears splitting the curves into two regions. In the first one, the low frequencies region, the end time is lower than the period of the signal applied and %D(t_{end}) quickly decreases as the frequency increase. After that, the slope abruptly changes and %D(t_{end}) decreases more smoothly because in this second region the end time becomes greater than the period of the external oscillation. Based on this behavior it could be concluded that, in general, the convective contamination is mainly due to the 'continuous part' of the gravity signal; removing it, the fluctuations do not affect the measure of the diffusion coefficient provided the frequency was high enough. It is interesting to mention also that the dimensional range of frequencies considered in our calculations is very low and that anti-vibratory mount strategies are more focused to damp vibrations of higher frequencies, in the vibratory range

(between 0.1 and 300 Hz following the NASA's definition concerning the International Space Station [44]). The inset of Fig. 6 corroborates the conclusions presented in the preceding cases about the different configurations and numerical methods.
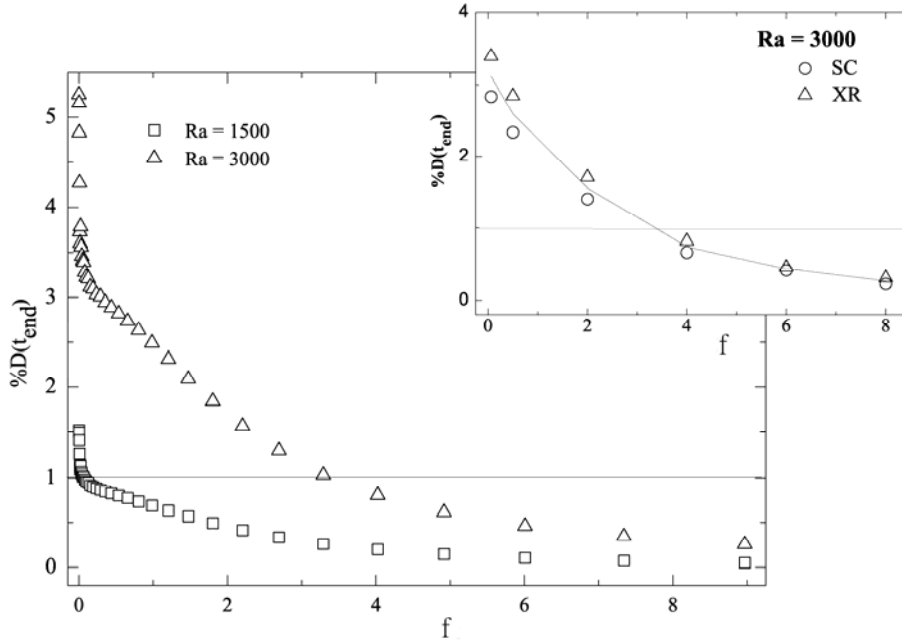

Fig. 6. Variation of the $\%D(t_{end})$ values as a function of the applied external harmonic frequencies for two different values of the Rayleigh number, Ra=1500 (triangles) and Ra=3000 (squares). In the inset figure, we show values of $\%D(t_{end})$ obtained modelling the two different experimental techniques SC and XR.
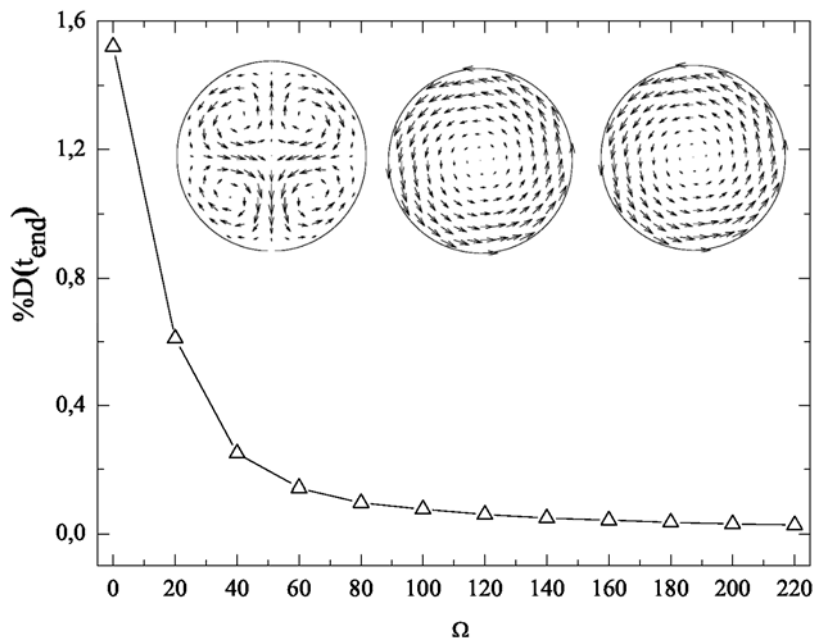
Fig. 7. $\%D(t_{end})$ for different non dimensional axial angular velocities, for a fixed Rayleigh number (Ra=1500). The insets represent the transversal velocity field at the cylinder center plane for $\Omega = 0$, $\Omega = 1$ and $\Omega = 100$. Note that the flow is already dominated by rotation for small values of Ω.

We have also analyzed the effect of the rotation around the axis of the cylinder of the cell in the determination of the diffusion coefficient %D(t_{end}). The results corresponding to a fixed value of the Rayleigh number (Ra=1500), maintaining the gravity field orthogonal to the initial concentration gradient, are depicted in Fig. 7. This figure clearly show how the error %D(t_{end}) significantly decreases as the rotation rate increases. In the same figure we have represented the transversal velocity field at the plane z = Γ/2 for the case without rotation, Ω = 0, and for Ω = 1 and 100. We can see that already for Ω = 1, the flow is dominated by the axial rotation of the cell. This has to be interpreted as that the rotation weakens the convection currents induced by the concentration differences and have a stabilizing effect. In order to better understand the stabilization mechanism, in Fig. 8 we have represented the maximum difference of the concentration in each plane or slice perpendicular to the cylinder axis, from the center (z = Γ/2) to the capillary end (z = Γ), the values reported correspond to the final state of the time evolution (t_{end}). As expected the maximum differences are observed near the center of the cell, where the initial concentration step is situated, and the maximum difference is reduced as the rotation rate increases due to the mixing induced by the azimuthal circulation of the fluid.
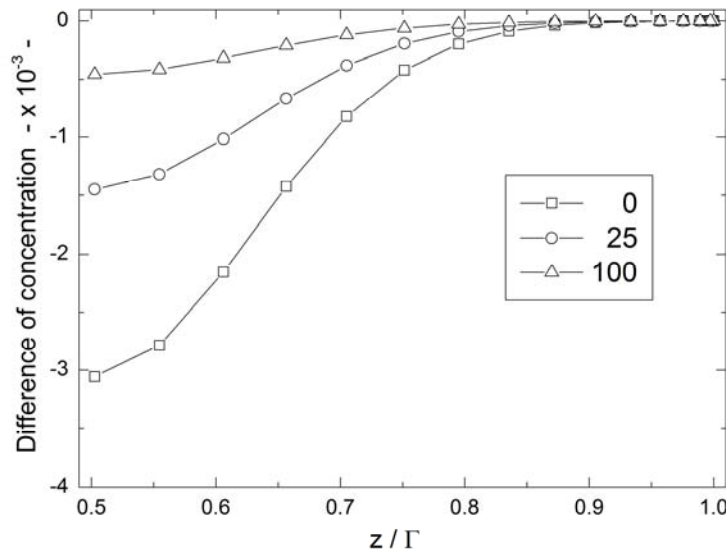
Fig. 8. Maximum difference of concentration at t=t_{end}, in the planes z=const. for Ω = 0 (squares), Ω = 25 (circles) and Ω = 100 (triangles). The concentration variations decrease significantly as the rotation rate is increased.

3.2. Implications on the International Space Station environment

The International Space Station, ISS, is the biggest and more complex orbiting object ever constructed in the space by the humanity till now. With a mass of about 455 Metric Tons moves at an average speed of 27700 Km/h (about 7.7 Km/s) describing an elliptical orbit around the Earth. The eccentricity of this orbit is 0.0012, the orbital inclination is about 51.64 degrees and the perigee and apogee are located at about 350 and 450 Km to the Earth's surface respectively (Low Earth Orbit, LEO, type). The orbital period is about 92 minutes, equivalently, the Station makes about 15.6 revolutions around the Earth per day. However, all these orbital details are time dependent because the atmospheric drag consequence of the friction with the surrounding atmosphere generates an orbital decay, in average, of about 150 m per day (the mean density of this outer atmosphere is of the order of 10^7 molecules/cm^3, but it also changes as a consequence of the solar

activity). So, periodical reboosts at intervals usually between ten and eighty days are mandatory to increase the velocity for continuous Orbital Adjustments, OA. Also reboosts – or deboosts to decrease the velocity - are used for Debris Avoidance Manoeuvres, DAM, or to prepare more efficiently the rendezvous with resupply or crew transport spacecrafts. Dockings and undockings as well as astro/cosmonaut spacewalks to build or repair parts of the Station configure a complete dynamic reality of that peculiar orbiting place [44 - 46].

To fix ideas and define thresholds, in the present work we concentrate on the last agitated period of the Station, 2009 – 2011. During this period the last Shuttle –Atlantis- undocked the Station in July the 19th of 2011 and during the above-mentioned triennium the Atlantis and the Endeavour docked the Station a total of three times each one, the Discovery docked four times and all together brought more than 150 Tones of modules and hardware to complete the Station [47 – 56]. Also, the spacecrafts used for OA / DAM were different, i.e., Progress, ESA Automated Transfer Vehicles, different Shuttles and, sporadically, the Zvezda or the Zarya modules. Aiming to quantitatively investigate the accelerometric impact of these spacecrafts, we have firstly downloaded their corresponding quasi steady fingerprints from the MAMS ossbtmf sensor located in the Destiny module from PIMS NASA website [57]. The signals downloaded are originally trimmed filtered and bias compensated. The sampling rate is in all cases 0.0625 Hz and the cut-off frequency 0.01Hz [58]. We concentrate here in the low frequency range because, from the point of view of fluid mechanics in general, this is the most pernicious one [59, 60]. In addition, recent literature indicates that the vibratory range –equivalently SAMS signals- do not impact in a relevant way the diffusion coefficient measurements at all [61 - 64]. Mention finally that the rest of disturbances, dockings, undockings and Extra Vehicular Activities show accelerometric levels considerably lower than the OA / DAM ones, so they have been initially discarded.

The reference used here to quantify the problem is the Space Station Analysis coordinate system, SSA. This is an orthonormal one with the Z_A axis pointing toward the center of the Earth (Nadir direction). The X_A axis coincides with the line of manned modules and YA axis coincides with the line of the Integrated Truss Structure, ITS. The X_A axis is considered positive, +XA, going from the Zvezda to the Harmony modules. In the same way, the Y_A axis is considered positive going from the P6 to the S6 Truss Segments [44 - 46], [65]. The origin of coordinates is located in the center of mass of the Station, a point actually located in the S0 Truss segments. To characterize the different signals we use their g-doses in m/s related to the above-mentioned SSA reference. In this way, the g-dose corresponding to the X_A component is defined as $\delta a_{X_A}(t) = \int_{t}^{t+\tau_i} |a_x(t)| \cdot dt$

and, because its own definition, it is equivalent to the variation of velocity in this period of time, Δv, a typical measure of the change of velocity used for fly controllers in Orbiter Adjustments. Fig. 9 shows that during the three-year period under study the maximum positive values of the X_A accelerometric doses for Progress and ATV spacecrafts are of the same order than the Zarya or Zvezda ones, however, the thruster ignition time, τ_i, is higher in the two first cases as a consequence of the resupply character of both spacecrafts. In the case of the five Shuttle reboosts the values are considerably lower than rest of spacecrafts. This is because only the Reaction Control System, RCS, was used for OA / DAM. This system comprises three groups of primary and Vernier small jets located in the forward fuselage and in two independent pods located on each side of the vertical tail of the orbiter's aft fuselage. The pods also house the aft Orbital Maneuvering System, OMS, and were usually referred as the OMS / RCS pods. Concerning the g-doses corresponding to the Y_A and Z_A-axes, say only that the values are, in all cases, very low against the corresponding X_A ones, so, their impact will be very small.
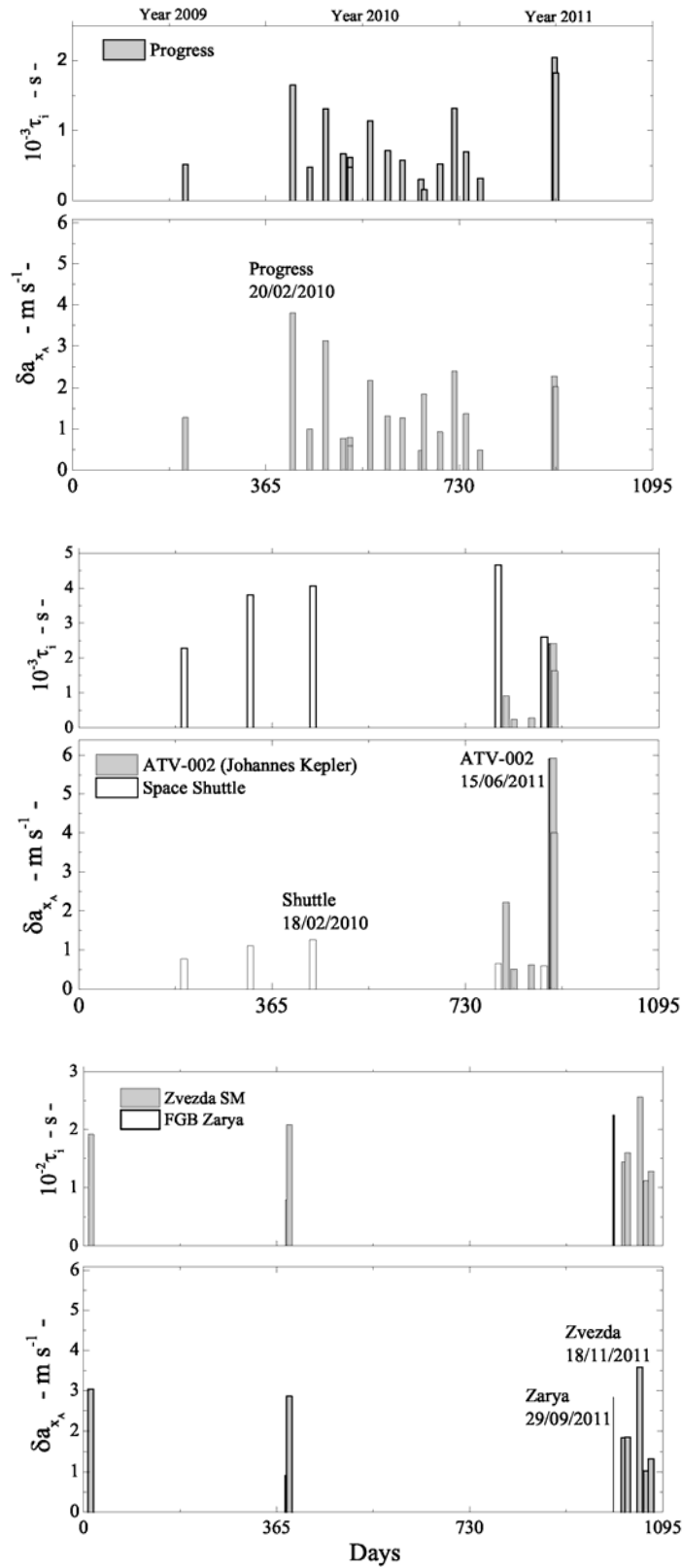
Fig. 9. G-doses corresponding to the X_A component of the different spacecrafts considered in the present study during the triennium 2009 - 2011.
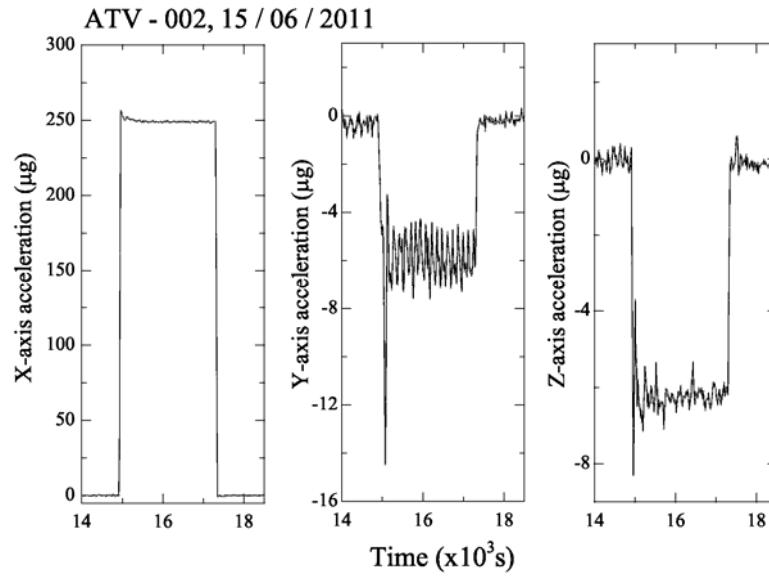
Fig. 10. SSA cartesian accelerometric components of a real reboosts finally selected (quasi-steady range)

Based on the information summarized in Fig. 9 and in order to analyze the impact of the OA / DAM manoeuvers on the accuracy of the measurements of the diffusion coefficients, we selected five scenarios, one for each spacecraft, with high values of the X_A g-dose. Fig. 10 explicitly shows, as an example, one of the five quasi-steady signals selected. The three accelerometric components of the signals have been introduced in the two 3D computational schemes, finite volumes and pseudospectral, taking into account that the signal of the X_A sensor was applied to the Z axis of the shear cell. In addition to be as exhaustive as possible each scenario activates the perturbation at different times of the diffusion process. Fig. 11 clarifies the four situations concerning only the acceleration introduced in the Z axis. The other two components of acceleration were activated for calculations at the same time as X_A was. Final results are synthesized in Table 3 but only in the case of Al-based alloys (the PV-Si melt is similar). It could be noted that despite the impact of the reboosts is practically negligible in all cases, that is to say, the values are always below the resolution limits of the experiments, a slightly increase of the percentage of error seems to exist as a function of the instant of time at which the perturbation is applied. This is a consequence of the fact that the flow has increasingly less time to relax the impact of the different reboosting episodes. Mention finally that because the rest of disturbances have small accelerometric levels, from the present analysis it could be concluded that these kinds of disturbances have definitively no impact on the accuracy of the diffusion coefficient measurements effected in either case, doped PV-Si melts or Al-based alloys.
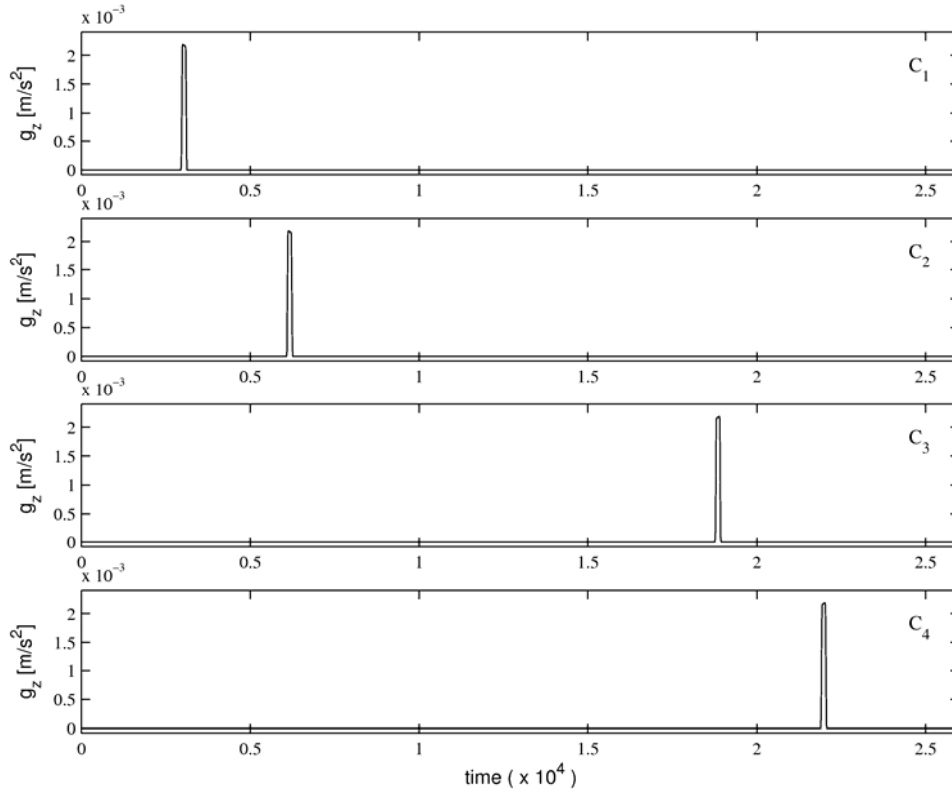
Fig. 11. The four different cases, C1, C2, C3 and C4 considered in the present work for the activation of the accelerometric signal.

	C1	*C2*	*C3*	*C4*
Progress	0.001	0.001	0.002	0.004
	0.000	0.000	0.001	0.001
Shuttle	0.001	0.001	0.001	0.002
	0.000	0.000	0.000	0.001
ATV-002	0.001	0.002	0.003	0.008
	0.001	0.001	0.004	0.006
Zvezda	0.001	0.002	0.003	0.003
	0.000	0.001	0.002	0.002
Zarya	0.001	0.001	0.004	0.005
	0.005	0.005	0.007	0.008

Table 3. 3D results of the final %D(t_{end}) indicator for the different spacecrafts considered. In each cell the upper part shows the Finite Volume result while the lower part presents the results obtained using the pseudospectral code.

4. CONCLUSIONS

In this work the solutal convective effects in a cylindrical capillary fulfilled with liquid Al-based alloys or with doped photovoltaic silicon, have successfully been analyzed for low and moderate solutal Rayleigh

19

numbers. For one hand, we have used 3D finite volume code to gain experience in the simulation of the flow behavior of a twenty segment shear cell, for the other, a pseudospectral 3D code enabled us to calculate instantaneous and continuous concentration profiles all along the capillary. These profiles have been used, as it would have in real X-ray experiments, to estimate an apparent diffusion coefficient concerning melt dopants or two-component mixtures. Further numerical procedures report in both, shear cells and capillaries, the error introduced by the convective bulk flow generated by a number of different gravity conditions. Calculations indicate that, fortunately, the relevant disturbing thresholds are always located in the level of *mg*. In addition we have also analyzed in detail the effect of harmonic disturbances of very low frequencies. The results indicate that the behavior of %D(t_{end}), is always monotonically decreasing with the increasing in frequency. Also the effect of rotating the cell along the cylindrical axis has been proved to be an extremely effective way of suppressing the mass transport due to convection. The numerical simulations show exactly that %D(t_{end}) quickly diminishes as the angular velocity increases. Finally, we have discussed in detail how real microgravity conditions onboard the ISS during the last agitated period of building of the Station can affect the measurement of diffusion coefficients. The conclusion in both, shear cells and capillaries, is very favorable in the sense that even under the influence of these strongest ISS transient disturbances, no convective impact has been detected in all the calculations. Equivalently, the %D(t_{end}) values obtained are always far below the experimental limit of detection, the 1% threshold.

REFERENCES

[1] X. Ruiz, J. Pallarés, F.X. Grau, *On the Accuracy of the Interdiffusion Measurements at Low and Moderate Rayleigh Numbers. A Computational Approach*, International Journal of Heat and Mass Transfer, (2010) 53, 3708 – 3720.

[2] X. Ruiz, J. Pallarés, *On the accuracy of the diffusion coefficient measurements using different initial shear cell configurations at low and moderate Rayleigh numbers.* International Journal of Heat and Mass Transfer, 55 (2012). 6966 – 6978.

[3] A. Dario, H. O. Sicim, E. Balikci, *Germanium-silicon single cystal growth by the axial heat processing (AHP) technique,* Journal of Crystal Growth (2011) 318 1057 - 1061.

[4] A. Griesche, F. Garcia Moreno, M.-P, Macht, G. Frohberg, *Chemical diffusion experiments in AlNiCe-melts*, Materials Science Forum (2006) 508, 567 – 572.

[5] A. Griesche, B. Zhang, J. Horbach, A. Meyer, *Atomic diffusion and its relation to thermodynamic forces in Al-Ni melts*, Defects and Diffusion Forum (2009) 289-292, 705 – 710.

[6] B. Zhang, A. Griesche, A. Meyer, *Diffusion in Al-Cu melts studied by time-resolved X-ray radiography.* Physical Review Letters 104 (2010) 035902 – 035902-4.

[7] A.G. Ostrogorsky, *Numerical simulation of single crystal growth by submerged heater method,* Journal of Crystal Growth (1990) 104, 233-238.

[8] A.G. Ostrogorsky, G. Müller, *Normal and zone solidification using the submerged heater method*, Journal of Crystal Growth (1994) 137, 64 – 71.

[9] S.V. Bykova, V.D. Golyshev, M.A. Gonik, V.B. Tsevetossky, E. Balikci, A. Deal, R. Abbaschian, M.P. Marchenko, I. V. Frjazinov, V.N. Vlasov, J.A. Serebrjakov, *The experimental-numerical investigation of*

instability of faceted Ge doped by Sb growth on the base of AHP method, Journal of Crystal Growth (2005) 275 e229 - e236.

[10] M.A. Gonik, A.V. Lomokhova, M.M. Gonik, A.T. Kuliev, A.D. Smirnov, *Development of a model for on-line control of crystal growth by the AHP method,* Journal of Crystal Growth (2007) 303 180 - 186.

[11] M.P. Marchenko, V.D. Golyshev, S.V. Bykova, *Investigation of $Cd_{1-x}Zn_x$ composition inhomogeneity at crystal growth by AHP-method,* Journal of Crystal Growth (2007) 303 193 - 198.

[12] B.V. Tryggvason, R. F. Redden, R.A. Herring, W. M. B. Duval, R.W. Smith, K.S. Rezkallah, S. Varma, *The vibration environment on the International Space Station: its significance to fluid-based experiments,* Acta Astronautica (2001) 46, 59 - 70.

[13] R. Savino, D. Paterna, *Compatibility of the microgravity environment of the International Space Station with fluid and material science experimentation,* Acta Astronautica (2002) 51, 229 - 241.

[14] R. Monti, R. Savino, D. Paterna, The fluid-dynamic disturbances induced on the ISS, based on the first acceleration measurements on board the space station, Acta Astronautica (2005) 57, 22 - 30.

[15] R. Monti, R. Savino, D. Paterna, *On a more rational specification for the microgravity environment of the International Space Station,* Acta Astronautica (2006) 58, 197-208.

[16] F. Barvinschi, C. Stelian, Y. Delannoy, N. Mangelinck, T. Duffar, *Modelling the multi-crystalline silicon ingot solidification process in a vertical square furnace,* Journal of Optoelectronics and Advanced Materials (2003) 5, 293 – 300.

[17] Y. Delannoy, F. Barvinschi, T. Duffar, *3D dynamic mesh numerical model for multi-crystalline silicon furnaces*, Journal of Crystal Growth (2007) 303, 170 – 174.

[18] D. Vizman, J. Friedrich, G. Mueller, *3D time-dependent numerical study of the influence of the melt flow on the interface shape in a silicon ingot casting process*, Journal of Crystal Growth (2007) 303, 231 - 235.

[19] B. Wu, N. Stoddard, R. Ma, R. Clark, *Bulk multicrystalline silicon growth for photovoltaic (PV) application*, Journal of Crystal Growth (2008) 310, 2178 – 2184.

[20] A.T. Kuliev, N.V. Durnev, V.V. Kalaev, *Analysis of 3D unsteady melt flow and crystallization front geometry during a casting process for silicon solar cells*, Journal of Crystal Growth (2007) 303, 238 – 240.

[21] L. Liu, S. Nakano, K. Kakimoto, *Dynamic simulation of temperature and iron distributions in a casting process for crystalline silicon solar cells with a global model*, Journal of Crystal Growth (2006) 292, 515 – 518.

[22] H. Matsuo, R.B. Ganesh, S. Nakano, L. Liu, Y. Kangawa, K. Arafune, Y. Ohshita, M. Yamaguchi, K. Kakimoto, *Thermodynamical analysis of oxigen incorporation from quartz crucible during solidification of multicrystalline silicon for solar cell,* Journal of Crystal Growth 310 (2008) 4666 – 4671.

[23] B. Gao, X.J. Chen, S. Nakano, K. Kakimoto, *Crystal growth of high-purity multicrystalline silicon using a unidirectional solidification furnace for solar cells,* Journal of Crystal Growth 312 (2010) 1572 – 1576.

[24] N. Dropka, W. Miller, R. Menzel, U. Rehse, *Numerical study on transport phenomena in a directional solidification process in presence of travelling magnetic field,* Journal of Crystal Growth 312 (2010) 1407 – 1410.

[25] T. Liu, Z. Dong, Y. Zhao, J. Wang, T. Chen, H. Xie, J. Li, H. Ni, D. Huo, *Purification of metallurgical silicon through directional solidification in a large cold crucible,* Journal of Crystal Growth 355 (2012) 145 – 150.

[26] Ch. -A. Gandin, J. –L. Desbiolles, M. Rappaz, Ph. Thevoz, *A three-dimensional cellular automaton-finite element model for the prediction of solidification grain structures,* Metallurgical and Materials Transactions A, 30 (1999) 3153 – 3165.

[27] J. Friedrich, R. Backofen, G. Müller, *Numerical simulation of formation of grain structure and global heat transport during solidification of technical alloys in MSL inserts,* Advanced Space Research (2002) 29, 549–662.

[28] B. Wu, S. Scott, N. Stoddard, R. Clark, A. Sholapurwalla, *Simulation of silicon casting process for photovoltaic (PV) application,* The Mineral, Metals & Materials Society, 2009.

[29] L. Liu, S. Nakano, K. Kakimoto, *Dynamic simulation of temperature and iron distributions in casting process for crystalline silicon solar cells with a global model,* Journal of Crystal Growth (2006) 292, 515-518.

[30] D. Vizmann, *3D time-dependent numerical study of the influence of the melt flow on the interface shape in a silicon ingot casting process*, Journal of Crystal Growth (2007) 303, 231-235.

[31] J.P. Garandet, *New determinations of Diffusion Coefficients for various dopants in liquid silicon,* International Journal of Thermophysics (2007) 28, 1285-1303.

[32] K.-H. Lee, *Axial distribution of Gallium and Silicon crystals for photovoltaic applications,* Japanese Journal of Applied Physics (2007) 46, 2831-2854.

[33] J. Brillo, I. Egry, J. Westphal, *Density and thermal expansion of liquid binary Al-Ag and Al-Cu alloys*, International Journal of Matterial Research, (2008), 99, 162-167.

[34] A. Griesche, B. Zhang, J. Horbach, A, Meyer, *Atomic diffusion and its relation to thermodynamic forces in Al-Ni melts,* Defect and Diffusion Forum (2009) 289-292, 705-710.

[35] J. P. Garandet, G. Mathiak, V. Botton, P. Lehmann, A. Griesche, *Reference microgravity measurements of liquid phase solute diffusivities in Tin- and Aluminum-based alloys*, International Journal of Thermophysics (2004) 25, 249-272.

[36] A. Griesche, F. García-Moreno, M. –P Macht, G. Frohberg, *Chemical diffusion experiments in AlNiCe-melts*, Materials Science Forum (2006) 508, 567-572.

[37] J. Pallarés, I. Cuesta, F.X. Grau, *Laminar and turbulent Rayleigh-Bénard convection in a perfectly conducting cubical cavity*, International Journal of Heat and Fluid Flow, 23 (2002) 346 – 358.

[38] Numerical Recipes: The Art of Scientific Computing, Cambridge University Press, 2007.

[39] I. Mercader, O. Batiste, A. Alonso, *An efficient spectral code for incompressible flows in cylindrical geometries*, Computers and Fluids, 39 (2010) 215–224.

[40] S. Hugues S, A. Randriamampianina . *An improved projection scheme applied to pseudospectral methods for the incompressible Navier-Stokes equations.* nt. J. Numer. Methods Fluids, 28,(1998), 501-521.

[41] G.E. Karniadakis, M. Israeli, S.A. Orszag, *High Order Splitting Methods for the Incompressible Navier-Stokes Equations.* J. Comput. Phys., 97 (1991) 414-443.

[42] B. Fornberg, *A Practical Guide to Pseudospectral Methods*. Cambridge University Press; 1998.

[43] L.N. Trefethen LN. *Spectral Methods in Matlab*. SIAM; 2000.

[44] K. Jules, *Working in a Reduced-gravity Environment: A Primer*, NASA 7th Annual Microgravity Environment Interpretation Tutorial, NASA Glenn Research Center, Ohio Aerospace Institute, Cleveland, Ohio. 2004.

[45] E. Ceglia, *European Users Guide to Low Gravity Platforms*, UIC-ESA-UM-0001. Issue 2 Revision 0, 2005.

[46] *Reference guide to the INTERNATIONAL SPACE STATION*, Assembly Complete Edition, November 2010. NASA Document NP-2010-00-682 HQ.

[47] http://www.nasa.gov/pdf/304681main_STS-119_Press_Kit.pdf (STS 119, Press Kit, February 2009. NASA)

[48] http://www.nasa.gov/pdf/358018main_sts127_press_kit.pdf (STS-127, Press Kit, June 2009, NASA)

[49] http://www.nasa.gov/pdf/379392main_STS-128_Press_Kit.pdf (STS-128, Press Kit, August 2009. NASA)

[50] http://www.nasa.gov/pdf/397216main_sts129_presskit.pdf (STS-129, Press Kit, October 2009. NASA)

[51] http://www.nasa.gov/pdf/423514main_sts130_press_kit_2.pdf (STS-130, Press Kit, January 2010. NASA)

[52] http://www.nasa.gov/pdf/435885main_sts131_press_kit.pdf (STS-131, Press Kit, April 2010. NASA)

[53] http://www.nasa.gov/pdf/451029main_sts132_press_kit2.pdf (STS-132, Press Kit, May 2010. NASA)

[54] http://www.nasa.gov/sites/default/files/files/491387main_STS-133.pdf (STS-133, Press Kit, February 2011. NASA)

[55] http://www.nasa.gov/mission_pages/shuttle/shuttlemissions/sts134/ (STS-134, Press Kit, April 2011. NASA)

[56] http://www.nasa.gov/pdf/566071main_135_press_kit2.pdf (STS-135. Press Kit, July 2011. NASA)

[57] http://pims.grc.nasa.gov/html/ISSAccelerationArchive.html

[58] E. Kelly, *International Space Station (ISS) Measured Quasi-Steady Environment,* NASA 7th Annual Microgravity Environment Interpretation Tutorial, NASA Glenn Research Center, Cleveland, Ohio, 2004.

[59] E. Nelson, *Predicting Residual Acceleration Effects on Space Experiments,* NASA 7th Annual Microgravity Environment Interpretation Tutorial, NASA Glenn Research Center, Cleveland, Ohio, 2004.

[60] A. Ahadi, M.Z. Saghir, *Quasi Steady State Effect of Micro Vibration from Two Space Vehicles on Mixture During Thermodiffusion Experiment,* Fluid-Dynamics and Material Processing 8 (2012) 397 – 422.

[61] Y. Yan, S. Pan, K. Jules, M.Z. Saghir, *Vibrational effect on thermal diffusion under different microgravity environments,* Microgravity Science and Technology XIX-2 (2007) 12 - 24.

[62] A. Ahadi, M.Z. Saghir, *Transient Effect of Micro Vibration from Two Space Vehicles on Mixture During Thermodiffusion Experiment,* Microgravity Science and Technology 25 (2013) 127 - 139.

[63] N. Sáez, X. Ruiz, J. Pallarés, V. Shevtsova, *On the accuracy of the interdiffusion coefficient measurements of high temperature binary mixtures under real ISS conditions*. Comptes Rendus Mècanique, 341 (2013) 405-416.

[64] A. Khoshnevis, A. Ahadi, M.Z. Saghir, *Influence of Static and Oscillatory gravity fields on thermodiffusion of a binary mixture*, International Journal of Thermal Sciences 75 (2014) 221 – 232.

[65] K. Jules, K. Hrovat, E. Kelly, T. Reckart, *International Space Station Increment -6/8. Microgravity Environment*. Summary Report, 2006 (NASA TM-2006-213896).